Information in Engineering Conference
IDETC/CIE 2007
September 4-7, 2007, Las Vegas, Nevada, USA

DETC2007-34130

TRANSVERSE VIBRATION INSTABILITIES IN MULTIRIBBED BELT TRANSMISSION SUBJECTED TO MULTI-FREQUENCY EXCITATIONS: MODELLING AND EXPERIMENTS.

Guilhem Michon *

Laboratoire LMS, SUPAERO,
10 avenue Édouard-Belin,
F31055 Toulouse, France
guilhem.michon@supaero.fr

Lionel Manin
Didier Remond
Regis Dufour
LaMCoS, INSA-Lyon, CNRS UMR5259
18 rue des Sciences,
F69621 Villeurbanne, France

Robert G. Parker

Ohio State University
Scott Lab
201 W 19TH AVE
Columbus, OH 43210

ABSTRACT

This paper experimentally investigates the parametric instability of an industrial axially moving belt subjected to multi-frequency excitation. Based on the equations of motion, an analytical perturbation analysis is achieved to identify instabilities. The second part deals with an experimental set-up that subjects a moving belt to multi-frequency parametric excitation. A data acquisition technique using optical encoders and based on the angular sampling method is used with success for the first time on a non-synchronous belt transmission. Transmission error between pulleys, pulley/belt slip and tension fluctuation are deduced from pulley rotation angle measurements. Experimental results validate the theoretical analysis. Of particular note is that the instability regions are shifted to lower frequencies than the classical ones due to the multi-frequency excitation.

INTRODUCTION

Instead of classical V-belts, serpentine drives are used in front end accessory drives (FEAD). They use flat and multi-ribbed belts running over multiple accessory pulleys, leading to simplified assembly and replacement, longer belt life and compactness [1]. Numerous mechanical phenomena occur in this application: rotational vibrations [2], hysteretic behavior of belt tensioner [3], nonlinear transverse vibration due the existence of pulley eccentricity [4], dry friction tensioner behavior [5], or parametric excitation.

Commonly known under the category of axially moving media, belt spans are subjected to parametric excitation from their operating environment as studied by Zhang [6]. A theoretical nonlinear dynamic analysis is also analyzed by Mockenstrum et al. [7, 8]. But only Pellicano et al. [9, 10] present a coupled theoretical and experimental investigation, where the excitation comes from pulley eccentricity which causes simultaneous direct and parametric excitation.

Widely used in automotive engines, belt spans experience multi-frequency excitation caused by engine firing and accessory variable torques [11]. Belt parametric instability occurs as transverse vibration in these applications, where the problems are noise and belt fatigue.

This paper builds on a previous work of Parker and Lin [12] as an experimental illustration and model validation. First, it deals with the general moving belt model subjected to multi-frequency tension and speed fluctuations. Then a specific test bench is presented, which produce this kind of excitation. Data acquisition is based on the principle of pulse timing method and leads to angular sampling for frequency analysis [13]. This method is applied here for the first time on a non-discrete geometry. The theoretical results from perturbation analysis are

*Address all correspondence to this author.

compared with the experimental ones.

MATHEMATICAL MODEL

A mathematical model of an axially moving beam subjected to multi-frequency tension and speed parametric excitation is used to establish the parametric instability region transition curves. The equation of motion for transverse vibration of a beam of length L moving with time dependent transport velocity $c(T)$ is governed by [14]

$$\rho A\left(V_{,TT}+c_{,T}V_{,X}+2cV_{,TX}+c^2V_{,XX}\right) - \left(P_s+P_d(T)\right)V_{,XX}+EIV_{,XXXX}=0 \quad (1)$$

where ρA is the mass per unit length, EI the bending stiffness, V the transverse displacement, P_s the mean belt tension, $P_d(T)$ the dynamic tension, and T and X the independent time and spatial variables. The dynamic tension results from longitudinal motion of the endpoints as a result of pulley oscillations and quasi-static mid-plane stretching from transverse deflection, and is given by

$$P_d(T)=\frac{EA}{L}\left[U(L,T)-U(0,T)+\frac{1}{2}\int_0^L V_{,X}^2\,dX\right] \quad (2)$$

where EA is the longitudinal stiffness modulus and U the longitudinal displacement. With the dimensionless parameters,

$$x,v,u=\frac{X,V,U}{L},\ t=T\sqrt{\frac{P_s}{\rho AL^2}},\ \gamma=c\Big/\sqrt{\frac{P_s}{\rho A}},$$
$$\zeta=\frac{EA}{P_s},\ \mu=\frac{EI}{P_sL^2},\ \Omega_i=\sqrt{\frac{\rho AL^2}{P_s}}\tilde{\Omega}_i \quad (3)$$

(1) becomes

$$v_{,tt}+2\gamma v_{,tx}+\gamma_{,t}v_{,x}-\left(1-\gamma^2\right)v_{,xx}+\mu v_{,xxxx} - \zeta\left[u(1,t)-u(0,t)+\frac{1}{2}\int_0^1 v_{,x}^2\,dx\right]v_{,xx}=0 \quad (4)$$

The belt tension and speed fluctuations are respectively

$$\zeta\left[u(1,t)-u(0,t)\right]=\sum_{i=1}^{k}\varepsilon_i\cos\left(\Omega_i t+\theta_i\right) \quad (5)$$

$$\gamma=\gamma_0+\sum_{i=1}^{k'}\varepsilon_i'\cos\left(\Omega_i' t+\theta_i'\right) \quad (6)$$

where $\varepsilon_i=EAu_i/P_s<1$ represents the ratio of the i^{th} spectral component of the dynamic tension fluctuation to the mean span tension.

As investigated in [12], the boundaries of the instability regions can be obtained on the basis of Floquet theory and perturbation analysis.

Linearizing equation (4) and writing in state space form gives [12]

$$AW_t+BW+\sum_{i=1}^{k'}\varepsilon_i'\left\{\sin\left(\Omega_i' t+\theta_i'\right)C+\Omega_i'\cos\left(\Omega_i' t+\theta_i'\right)D\right\}W - \sum_{i=1}^{k}\varepsilon_i\cos\left(\Omega_i t+\theta_i\right)EW+\left(\sum_{i=1}^{k'}\varepsilon_i'\sin\left(\Omega_i' t+\theta_i'\right)\right)^2EW=0 \quad (7)$$

where

$$A=\begin{bmatrix}1 & 0\\ 0 & -\left(1-\gamma_0^2\right)\frac{\partial^2}{\partial x^2}+\alpha\frac{\partial^4}{\partial x^4}\end{bmatrix},$$
$$B=\begin{bmatrix}2\gamma_0\frac{\partial}{\partial x} & -\left(1-\gamma_0^2\right)\frac{\partial^2}{\partial x^2}+\alpha\frac{\partial^4}{\partial x^4}\\ \left(1-\gamma_0^2\right)\frac{\partial^2}{\partial x^2}-\alpha\frac{\partial^4}{\partial x^4} & 0\end{bmatrix},$$
$$C=\begin{bmatrix}2\frac{\partial}{\partial x} & 2\gamma_0\frac{\partial^2}{\partial x^2}\\ 0 & 0\end{bmatrix},D=\begin{bmatrix}0 & \frac{\partial}{\partial x}\\ 0 & 0\end{bmatrix},E=\begin{bmatrix}0 & \frac{\partial^2}{\partial x^2}\\ 0 & 0\end{bmatrix},W=\begin{bmatrix}v_{,t}\\ v\end{bmatrix}. \quad (8)$$

The inner product in the state space is $\langle W,V\rangle=\int_0^1 W^T\overline{V}\,dx$, where overbar denotes complex conjugate and superscript T denotes transpose. The Galerkin basis consists of the state-space eigenfunctions of the non-parametrically excited moving string ($\mu=0$) system [15]

$$\Phi_n=\begin{bmatrix}j\omega_n\psi_n\\ \psi_n\end{bmatrix}=\begin{bmatrix}\lambda_n\psi_n\\ \psi_n\end{bmatrix} \quad (9)$$

where ψ_n are the complex eigenfunctions of (4) and ω_n the natural frequencies

$$\psi_n=\frac{1}{n\pi\sqrt{1-\gamma_0^2}}e^{jn\pi\gamma_0 x}sin(n\pi x),\quad \lambda_n=jn\pi(1-\gamma_0^2) \quad (10)$$

Let us define $E_{nm}=\langle E\Phi_n,\Phi_m\rangle$ and $E_{\bar{n}m}=\left\langle E\overline{\Phi}_n,\Phi_m\right\rangle$, with similar relations for the C and D operators.

Using perturbation analysis to consider speed and tension fluctuations, primary instability occurs when

$$\Omega_l = \Omega_l' = 2\omega_n \pm \sqrt{\left(\varepsilon_l' \left|-jC_{\bar{n}n} + 2\omega_n D_{\bar{n}n}\right|\right)^2 + \left(\varepsilon_l \left|E_{\bar{n}n}\right|\right)^2} - \left|E_{\bar{n}n}\right|^2 \left[-\sum_{i=1, i\neq l}^{k} \varepsilon_i^2 \frac{2\omega_n}{\Omega_i^2 - 4\omega_n^2} + \frac{\varepsilon_l^2}{8\omega_n}\right] - \left|-jC_{\bar{n}n} + 2\omega_n D_{\bar{n}n}\right|^2 \left[-\sum_{i=1, i\neq l}^{k'} \varepsilon_i'^2 \frac{2\omega_n}{\Omega_i'^2 - 4\omega_n^2} + \frac{\varepsilon_l^2}{8\omega_n}\right] + \sum_{i=1}^{k'} \left(\frac{\varepsilon_i'}{2}\right)^2 \left|E_{nn}\right| \quad (11)$$

and secondary instability occurs when

$$\Omega_l = \Omega_l' = \omega_n \pm \left[\left(\frac{\varepsilon_l^2}{\omega_n} Im(E_{nn}) \left|E_{\bar{n}n}\right|\right)^2 + \left(\frac{\varepsilon_l'^2}{\omega_n} Im(-jC_{nn} + \omega_n D_{nn}) \left|-jC_{\bar{n}n} + \omega_n D_{\bar{n}n}\right|\right)^2\right]^{1/2} - \left|E_{\bar{n}n}\right|^2 \left[-\sum_{i=1, i\neq l}^{k} \varepsilon_i^2 \frac{\omega_n}{\Omega_i^2 - 4\omega_n^2} + \frac{\varepsilon_l^2}{3\omega_n}\right] - \left|-jC_{\bar{n}n} + \omega_n D_{\bar{n}n}\right|^2 \left[-\sum_{i=1, i\neq l}^{k'} \varepsilon_i'^2 \frac{\omega_n}{\Omega_i'^2 - 4\omega_n^2} + \frac{\varepsilon_l^2}{3\omega_n}\right] + \sum_{i=1}^{k'} \left(\frac{\varepsilon_i'}{2}\right)^2 \left|E_{nn}\right| \quad (12)$$

EXPERIMENTAL SETUP

In industrial applications, excitation sources are not at a single frequency, especially in an automotive engine. Engine firing and driven accessories cause multi-frequency speed and tension fluctuations. Furthermore, practical belt speeds are such that they impact the dynamics and must be included. The following experiment examines parametric instabilities from this kind of excitation in a moving belt system.

Belt drive description

The studied transmission consists of four pulleys linked together by an automotive multi-ribbed belt, as shown in Fig. 1. The input shaft speed (from 0 to 2000 rpm) is controlled by a 60 kW electric motor. The driven shaft is connected to a hydraulic pump. The output pressure of the fluid is controlled to apply a mean torque on the driven pulley. Due to its design, however the pump generates torque fluctuations of order 2 (i.e., 2 pulses/rev) around the mean value. These fluctuations cause tension variations that parametrically excite the moving belt.

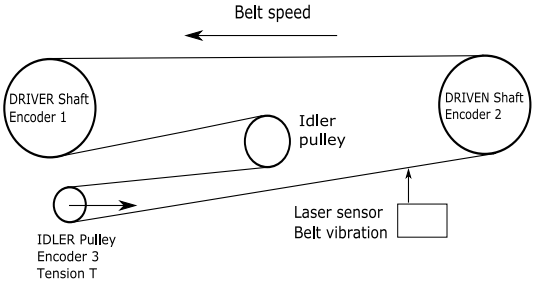

(a)

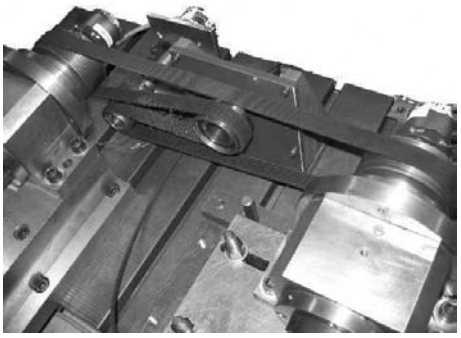

(b)

Figure 1. Experimental set-up for parametrically excited moving belt drive.

Figure 2. Example of instability in slack belt span

Due to the rotation direction, the upper span is tight and the lower one is slack. As these two spans have approximately the same length, the instability will appear in the slack span for the lowest excitation frequencies. Figure 2 shows an example of transverse vibration of the lower span.

Measurement devices

Angular positions are measured by optical encoders mounted on pulleys 1, 2 and 3 (respectively, 2048, 2048 and 2500 pulses/rev). Belt tension is measured by a piezo-electric sensor

on the pulley 3 support, and belt lateral vibration by a laser displacement sensor (0.02 m range, 10 μm dynamic resolution).

The data acquisition system is custom made with a PXI frame including classical data acquisition boards and a four-channel counter board permitting the use of the pulse timing method. Each optical encoder delivers a square signal (TTL) as it rotates. Between two rising edges of this signal, a counter records the number of pulses given by a high frequency clock (80 MHz), see Fig.3. For each encoder, it is therefore possible to build a time vector that contains the times of occurence of the TTL signal's rising edges. Hence, the total rotation angle of each shaft is determined and instantaneous rotation speed and acceleration are deduced. In this application, measurement is triggered on the reference encoder mounted on the driving shaft and analog signals are acquired at each instant of the reference encoder's rising edge. Obviously, when an analog signal is sampled in the angular domain, the speed conditions are taken into account in order to set the cut-off frequency of anti-aliasing filters. An important characteristic of this measurement principle is to separate resolution and precision. Resolution is given by the number of pulses per revolution, and the theoretical angular precision is proportional to the ratio between rotation speed and counter clock frequency. The grating quality of the optical encoder disk, as well as the electronic signal conditioning and processing may also affect the practical accuracy.

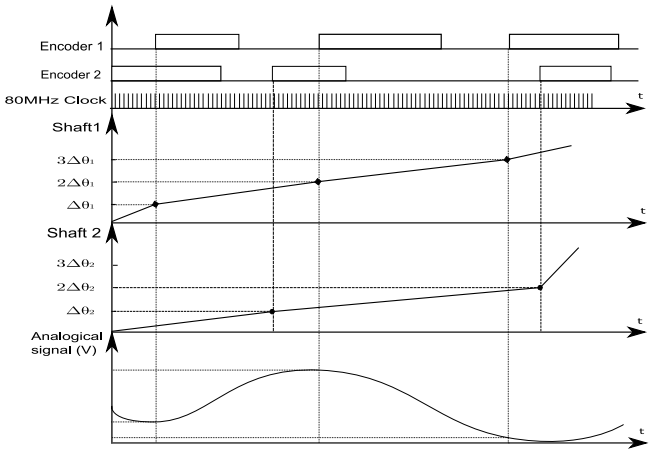

Figure 3. Angular sampling principle

Angular sampling benefits

Compared with classical acquisition [16], data are resampled based on the angular rotation of a chosen encoder which is not necessarily the reference one. It consists in calculating the angular rotations of the other encoders at the times corresponding to the rising edges of the sampling encoder. Hence, if angular sampling is performed on encoder i, the angular positions of each of the slave encoders are computed from linear interpolation at the times corresponding to the encoder i rising edge locations, see Fig. 5.

For the analog signals, the same method is applied and they are recorded at the angular frequency of the reference encoder. This method is called angular sampling and is detailed in [13]. It is mainly applied in rotating machines with synchronous transmission elements such as gears or timing belts. Its application to a transmission in the presence of belt slip is novel and provides important advantages as described below. This technique is especially useful for systems with variable speed because the position of the sampling points and the angular resolution remain exactly the same when the speed fluctuates.

As the angular sampling frequency is constant based on the encoder resolution, instead of performing the FFT analysis in the time domain, this is performed in the angular domain. In other words, the measured signals are treated as functions of the angular position of the sampling encoder. The sampling encoder's position plays the role typically filled by time in classical FFT analysis. The spectral data is a function of angular frequency, which has units of rad^{-1}. The maximum angular frequency is $\frac{1}{\delta\theta}$, where $\delta\theta = \frac{2\pi}{N_g}$ is the angular resolution of the sampling encoder based on N_g gratings. Increments on the angular frequency axis are spaced at $\delta f = \frac{1}{N \cdot \delta\theta}$ where N is the number of sampling encoder rising edges in the collected data. Examples of classical Campbell and angular frequency diagrams are compared in Figure 4. On Figure 4a , natural frequencies are located at a constant frequency when speed increases while speed-dependent frequency orders increase linearly. In the angular frequency domain, however, natural frequencies appear as hyperbola ($f = \omega \cdot \frac{1}{\theta}$) and speed-dependent frequency orders are located at a constant angular frequency ($f = a \cdot \omega$ leads to $\frac{1}{\theta} = a$), vertical lines parallel to the speed axis.

Thus, the main advantages of performing angular sampling in this application are:

- sampling points are exactly located in reference to the geometry of the rotating machine, even when speed varies. It permits to compare several measurement results based on the same sampling conditions.
- spectral analysis is always performed with the same accuracy and the same resolution. Angular sampling also insures that the magnitude of harmonic components are exactly estimated [13].
- by choosing the encoder 3 as reference, and assuming that no slip occurs between belt and the idler pulley since no torque is being transmitted, the sampling points are attached to the belt.

Therefore, it is more convenient to identify speed-dependent

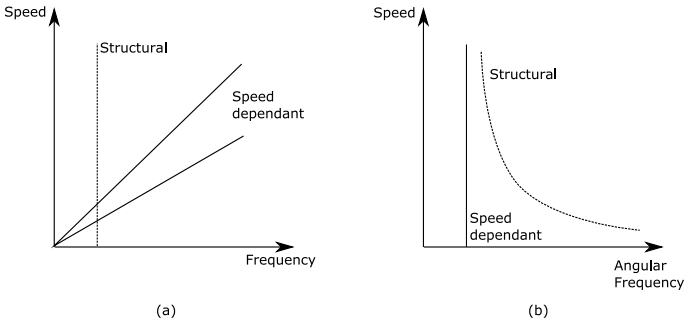

Figure 4. Campbell diagrams in (a) time and (b) angular frequency domain

frequency components on a graph with an angular frequency axis related to a chosen reference encoder.

For standard Fourier analysis, it is necessary to get the measurements as a function of one single time vector with equally spaced intervals. This requires a time re-sampling of the data using linear interpolation as shown in Fig. 5(b).

Phase difference measurement

This angular sampling method has already been used for many synchronous transmission studies (gearbox, timing belt drive) but never for non synchronous transmissions such as serpentine multi-ribbed belt drives. The transmission error ε is defined as the angular rotation difference between shaft i and shaft j,

$$\varepsilon = \theta_i - \eta \cdot \theta_j \tag{13}$$

where η and $\theta_{i,j}$ are respectively the transmission ratio and the angular positions of shaft $i,\ j$.

In the case of non-synchronous belt drive systems, some creep occurs between the belt and the pulleys due to the power transmission by friction [17, 18]. Indeed, the creep corresponds to the relative slip between the belt and the driven pulley as the belt elongates on the pulley contact arc as its tension increases. Here, the transmission error between pulleys 3 and 2 is considered. The rotation of pulley 3 is not totally transmitted to pulley 2 due to the belt stretching on pulley 2 which causes a delay. Therefore, the mean value of the transmission error is not zero as it is for a synchronous drive, but rather always increases (Fig.6). In our application, analysis permits decomposition of the observed transmission error as the sum of a linear function of time representing the transmission error due to pulley belt creep ε_{creep}, and the residual transmission error ε_{res} due to the system dynamic as in synchronous transmission.

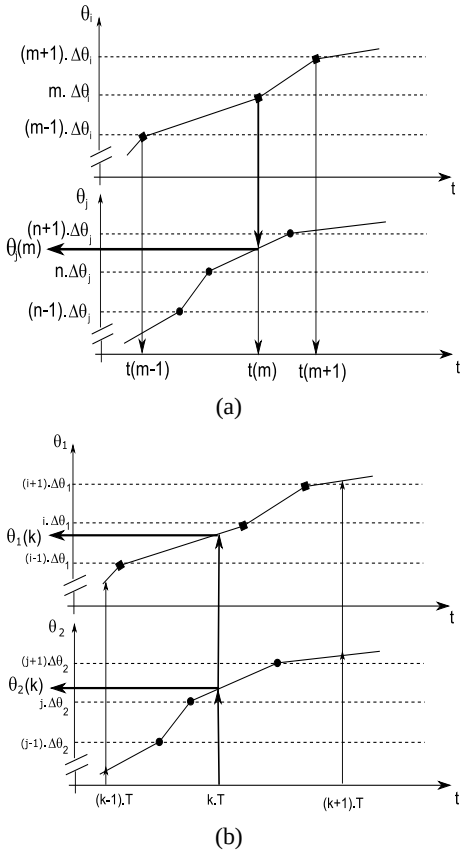

Figure 5. Angular re-sampling method(a) and Time re-sampling method (b).

$$\varepsilon = \theta_3 - \eta \cdot \theta_2 = \varepsilon_{res} + \varepsilon_{creep} \tag{14}$$

where ε_{creep} is identified from ε as a linear regression of time assuming a constant mean rotation speed. Removing the linear part ε_{creep} from the transmission error ε yields the zero-mean periodic residual transmission error ε_{res} (Fig. 6).

As mentioned in the theoretical model description, the dynamic belt tension can be expressed as the difference of the endpoint positions and mid-plane stretching from transverse vibration, see Equ. 2. Considering the belt span that connects pulleys 3 and 2, and taking into account the belt translation direction, $U(L,T)$ and $U(0,T)$ correspond respectively to the belt unseating point on pulley 3 and to the belt seating point on pulley 2. These two points are not fixed in space since pulley rotations oscillate around the linearly increasing angles $w_3 t$ and $w_2 t$. Assuming a no-slip condition at these two points, $U(L,T)$ and $U(0,T)$ can be estimated from pulley angle oscillations multiplied by the respective pulley pitch radius. Finally, the difference between

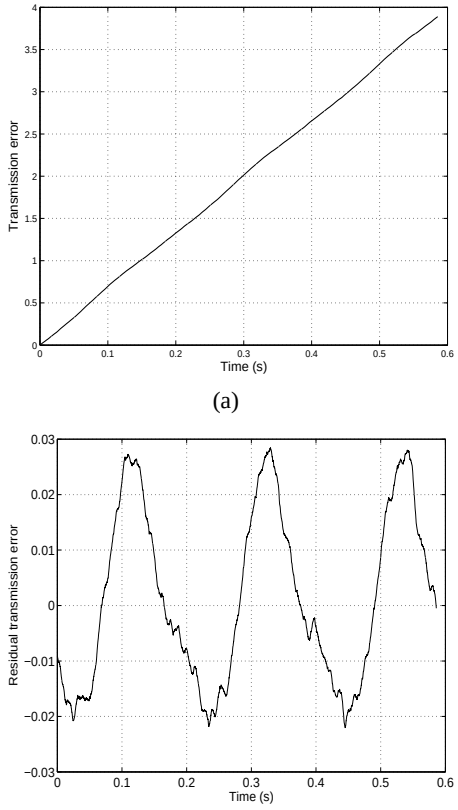

Figure 6. Total (a) and residual (b) transmission error versus time.

$U(L,T)$ and $U(0,T)$ corresponds to the residual transmission error at time T. Therefore, residual transmission error and belt tension fluctuation are related. Figure 7 presents the measured progression of belt tension and residual transmission error angular waterfall analysis with change in rotation speed (note that all waterfall plots are topviews). The same frequency components appear on each graph and prove that the measurement system with optical encoders and angular sampling permits evaluation of belt tension fluctuation. Finally, this analysis shows that the transmission error includes the pulley belt creep plus the system dynamic.

BELT SPAN INSTABILITY ANALYSIS

Experimental investigation

On the global experimental set-up for a given initial belt tension and mean torque, a speed sweep of the driving shaft is performed from 532 to 1512 rpm in 14 rpm increments (70 tests). The experimental results are presented in Fig. 8 as a top-view waterfall in the angular frequency domain for: (a) the

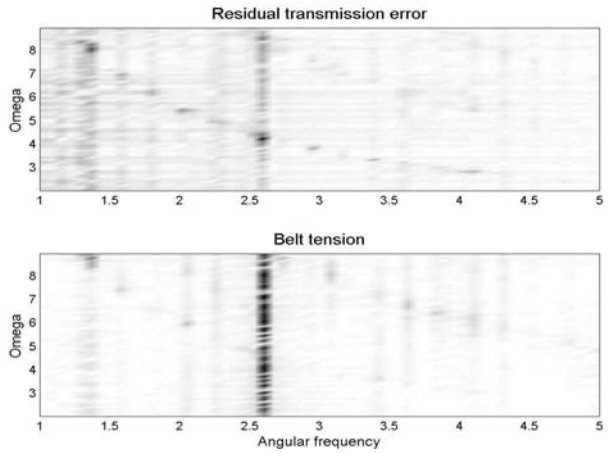

Figure 7. Belt tension and transmission error angular top-view waterfall as a function of rotation speed

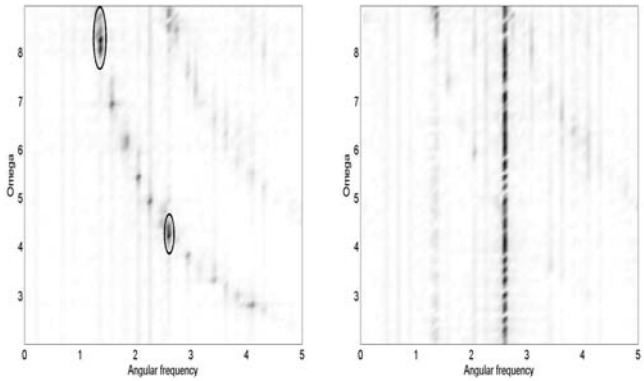

(a) (b)

Figure 8. Experimental angular top-view waterfall: (a) transverse vibration , (b) belt tension fluctuation. Circled areas of (a) highlight the instability regions.

transverse vibration , (b) belt tension and (c) belt speed . All parameters are dimensionless as defined in the first Section.

The belt tension angular waterfall, Fig.8(b), exhibits lines parallel to the speed axis, which proves a speed dependent excitation. The belt transverse vibration angular waterfall is presented on Fig.8(a). The instabilities are represented by the black spots located on a hyperbola. which proves parametric instability. The system is unstable for numerous frequencies.

Main instability regions

The main excitation of the system comes from the pump design which creates torque fluctuations of order 2, inducing speed

and tension fluctuations. Regarding belt instability, speed variation is a negligible source of excitation compared to the tension fluctuation. The latter is observed to be the principle source of parametric excitation and is located on the angular frequency waterfall graph at abscissa 2.60 as a vertical line. Primary and secondary instability regions, circled on Figure 8(a), are the response to this torque excitation.

Experimentally, the primary instability occurs for $\Omega_1 \in [7.9, 8.8]$. This region is classically wider than the corresponding secondary region (which occurs for $\Omega_1 \in [4.1, 4.5]$), but also shifted of 0.3 from $2\omega_1$ toward lower frequencies due to the multi-frequency excitation.

Considering the small transverse rigidity modulus and the large span length in this application, the bending stiffness modulus is neglected. Therefore, in the following, the belt span is considered as a string ($\mu = 0$). Thus, using Eq. (7) and (8) and $C_{\bar{n}n} = (1-e^{-2jn\pi\gamma_0})/2$, $D_{\bar{n}n} = 0$, $E_{\bar{n}n} = (1-e^{-2jn\pi\gamma_0})/(4\gamma_0)$, and $E_{nn} = jn\pi(1+\gamma_0^2)/2$. The experimental parameters introduced in the model are: $\gamma_0 = 0.5,\ \omega_1 = 4.3, \Omega_2 = 8,\ \Omega_2' = 8,\ \varepsilon_1' = 0.001,\ \varepsilon_2 = 0.3,\ \varepsilon_2' = 0.001$. For $\varepsilon_1 = 0.7$, the instability region occurs for $\Omega_1 \in [7.8 \quad 9.2]$.

The instability region boundaries are plotted as a function of the excitation amplitude ε_1 in Fig. 9. When $\Omega_2 < 2\omega_1$, the second source of excitation shift the instability region to lower frequencies. While this phenomenon is not classical, the experimental observations confirm the theoretical results of [12].

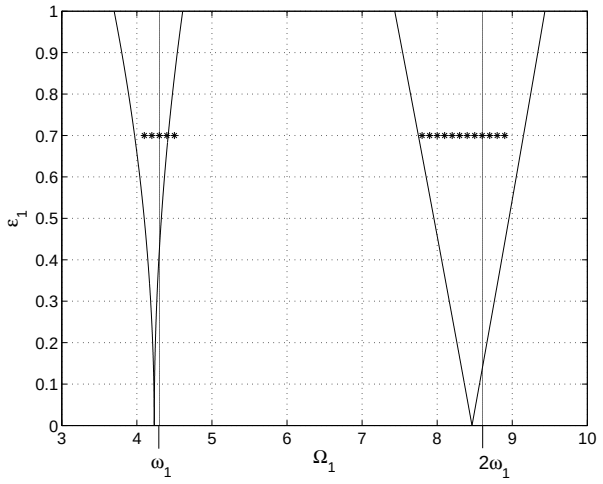

Figure 9. Instability region. Model (solid line) and experiment (stars).

CONCLUSION

This paper focuses on an experimental investigation of an industrial axially moving belt subjected to multi frequency excitation. Comparison with analytical results from a perturbation analysis is presented and permits to validate theoretical instabilities. The main conclusion are:

- Parametric instabilities occur in experimental system such as belt drive,
- Measurement system based on angular sampling is shown to be an efficient tool for instability analysis in belt drive systems,
- Instability regions are shifted when subjected to multi-frequency excitation,
- Experimental observations confirm the theoretical results.

Further analysis will focus on the role of the hysteretic behavior of the belt tensioners on these instabilities.

REFERENCES

[1] Gerbert, G., 1981. "Some notes on v-belt drives". *ASME - Journal of Mechanical Design*, **103**, pp. 8–18.

[2] Hwang, S., Perkins, N., Ulsoy, A., and Meckstroth, R., 1994. "Rotational response and slip prediction of serpentine belt dirve systems". *ASME - Journal of Vibration and Acoustics*, **116**, pp. 71–78.

[3] Michon, G., Manin, L., and Dufour, R., 2005. "Hysteretic behavior of a belt tensioner: Modeling and experimental investigation". *Journal of Vibration and Control*, **11**(9), pp. 1147–1158.

[4] Wickert, J., 1992. "Non-linear vibration of a traveling tensioned beam". *Int. J Non-linear Mechanics*, **27-3**, pp. 503–517.

[5] Leamy, M., and Perkins, N., 1998. "Nonlinear periodic response of engine accessory drives with dry friction tensioners". *ASME - Journal of Vibration and Acoustics*, **120**, pp. 909–916.

[6] Zhang, L., and Zu, J., 1999. "One-to-one auto-parametric resonance in serpentine belt drive systems". *Journal of Sound and Vibrations*, **232**, pp. 783–806.

[7] Mockensturm, E., Perkins, N., and Ulsoy, A., 1996. "Stability and limit cycles of parametrically excited, axially moving strings". *ASME - Journal of Vibration and Acoustics*, **118**, pp. 346–351.

[8] Mockensturm, E., and Guo, J., 2005. "Nonlinear vibration of parametrically excited viscoelastic axially moving media". *ASME - Journal of applied mechanics*, **72**, pp. 374–380.

[9] Pellicano, F., Catellani, G., and Fregolent, A., 2004. "Parametric instability of belts: theory and experiments". *Computer and Structures*, **82**, pp. 81–91.

[10] Pellicano, F., Fregolent, A., Bertuzzi, A., and Vestroni, F., 2001. "Primary and parametric non-linear resonances of a power transmission belt: experimental and theoretical analysis". *Journal of Sound and Vibration*, **244**, pp. 669–684.

[11] Cheng, G., and Zu, J., 2003. "Nonstick and stick-slip motion of a coulomb-damped belt drive system subjected to multifrequency excitations". *ASME - Journal of Applied Mechanics,* **70**, pp. 871–884.

[12] Parker, R., and Lin, Y., 2001. "Parametric instability of axially moving media subjected to multifrequency tension and speed fluctuation". *ASME - Journal of Applied Mechanics,* **68**, pp. 49–57.

[13] Remond, D., and Mahfoudh, J., 2005. "From transmission error measurements to angular sampling in rotating machines with discrete geometry.". *Shock and Vibration. IOS Press.,* **9**, pp. 1–13.

[14] Thurman, A., and Mote Jr, C., 1969. "Free, periodic, nonlinear oscillation of an axially moving string". *ASME - Journal of Applied Mechanics,* **36**, pp. 83–91.

[15] Jha, R., and Parker, R., 2000. "Spatial discretization of axially moving media vibration problems". *ASME- Journal of Vibration and Acoustics,* **122**, pp. 290–294.

[16] Houser, D., and Blankenshio, G., 1989. "Methods for measuring transmission error under load and at operating speeds". *SAE Transactions,* **98**(6), pp. 1367–1374.

[17] Gerbert, G., and Sorge, F., 2002. "Full sliding adhesive-like contact of v-belts". *ASME - Journal of Mechanical Design,* **124**, pp. 706–712.

[18] Betchel, S., Vohra, S., Jacob, K., and Carslon, C., 2000. "The stretching and slipping of belts and fibers on pulleys". *ASME - Journal of Applied Mechanics,* **67**, pp. 197–206.